Localised corrosion of iron and steel in the Callovo-Oxfordian porewater after 3 months at 120 °C: Characterizations at micro and nanoscale and formation mechanisms

Hélène Lotz, Delphine Neff, Florence Mercier-Bion, Christian Bataillon, Philippe Dillmann, Emmanuel Gardés, Isabelle Monnet, James Dynes, Eddy Foy

Localised corrosion of iron and steel in the Callovo-Oxfordian porewater after 3 months at 120°C: characterizations at micro and nanoscale and formation mechanisms

Hélène Lotz[1]*, Delphine Neff[1], Florence Mercier-Bion[1], Christian Bataillon[2], Philippe Dillmann[1], Emmanuel Gardés[3], Isabelle Monnet[3], James J. Dynes[4], Eddy Foy[1]

[1] LAPA, IRAMAT, NIMBE, CEA, CNRS, Université Paris-Saclay, CEA Saclay 91191 Gif-sur-Yvette France

[2] CEA, DEN, DPC/SCCME/LECA, Bât. 458, 91191 Gif-sur-Yvette, France

[3] Centre de Recherche sur les Ions, les Matériaux et la Photonique (CIMAP), CEA, CNRS, UCBN, ENSICAEN, Normandie Université, Caen, France

[4] Canadian Light Source Inc., University of Saskatchewan, Saskatoon, Saskatchewan, Canada

* Corresponding author: lotz.helene.lucie@gmail.com

Keywords

Steel, SEM, Raman, STXM/XANES, MET/SAED, localized corrosion, nuclear waste repository

Highlights

- Fe corrosion in Cox porewater leads to Fe carbonate, Fe silicate, Fe sulphate and Fe oxide formation.
- First step of Fe corrosion in Cox porewater is the formation of a Ca-siderite bi-layer
- Fe corrosion in Cox porewater continues locally at the M/CPL interface
- Local changes in the porewater chemistry led to a switch from a carbonate system to a mixed system

Abstract

To investigate the fate of nuclear waste in geologic repositories, corrosion experiments were performed on a ferrito-pearlitic (P285-NH) and a ferritic steel (Armco) in a synthetic solution representing the Callovo-Oxfordian porewater for 3-months at 120°C. Corrosion product layers (CPL) were characterized from micro to nanoscale. Local corrosion areas of higher thicknesses were composed of siderite layers with different nano-morphologies, iron silicate, iron sulphate and magnetite. Their formation could be due to local pH variation, but also on metal microstructure (phases location and morphology). Differences in corrosion progress are suggested to be mainly related to differences in porewater chemistry and cathodic sites.

Introduction

Iron and steel corrosion in a water saturated anoxic environment is a major issue in various fields [1–4] including the nuclear industry. In that latter context, steel is used as a part of the multibarrier for deep geologic repositories to confine high level nuclear wastes in several countries [5]. In the specific context of the French nuclear waste management, the host rock is a Callovo-Oxfordian (Cox) formation. Thus, the metal clay interface and its evolution were widely studied as its nature controls the corrosion rates of the steel. Different types of studies were developed for several years to gain insight into this interface and predict its behaviour. Integrated experiments following all environmental parameters of the host rock (mineralogy, pressure, temperature, porewater chemistry), allowed tracing the corrosion mechanism during several months to a few years [6]. Parametric experiments were developed to improve knowledge on the iron-environment interaction by reducing the number of parameters in order to target a corrosion mechanism [7–10]. Archaeological analogues were used to characterize the corrosion facies and estimate corrosion rates within centuries [11,12]. Modelling studies combined thermodynamic, electrochemical or metallurgical kinetic models or codes to validate experimental observations and/or predict the evolution of corrosion processes [13,14].

The overall behaviour of the iron-environment interface after several months tends towards the formation of a dense corrosion product layer which contains, from the environment to the metallic core : iron carbonate, iron silicate, iron sulphide and a more or less continuous layer of iron oxide at the Metal (M) / Corrosion Product Layer (CPL) interface [15–18]. A study involving two experiments carried out under similar conditions revealed that after one year, the decrease of the corrosion rate is higher for a ferritic steel compared to a ferrito-pearlitic steel [19]. This raised the question of the influence of the metal microstructure on the long-term corrosion rate of iron-based metals in anoxic environments. Another study [20] compared the corrosion facies obtained on a ferrito-pearlitic (P285-NH) and a ferritic steel (Armco). Corrosion experiments were performed during one month at 120°C in a synthetic solution representing the Callovo Oxfordian porewater. Both systems presented a Ca-siderite bilayer which interface locates the metal original surface, and nano to micrometric magnetite islets on the internal carbonated layer and at the M/CPL interface. The impact of cementite was highlighted in terms of morphology of the CPL with the presence of porosities and a higher CPL thickness (21 µm and 18 µm for the ferrito-pearlitic and the ferritic samples respectively).

From these experiments, it can be questioned whether the entire corrosion layer plays a role in the decrease of the corrosion rate or if the interfacial oxide layer is at the origin of this kinetic reduction as suggested by corrosion modelling studies [21] and characterized on several systems [22]. Indeed, the formation and properties of siderite has been widely studied in carbonate environment. Experiments in environmental conditions leading to a siderite layer with very low permeability were mainly performed at temperature above 70°C, pH 6 and few days exposure time [1,23–25]. As a consequence, it has been shown that $FeCO_3$ could act as a diffusion barrier to electrochemically active species, $CO_{2(aq)}$ and Fe^{+2}, and reduced the corrosion rate. In contrary, the iron silicate phases formed in purely silicate environment (MX 80 Bentonite, 120°C, 1 month or alkaline condition containing [SiO_2], 50°C, 1 month) appeared porous and poorly adherent to the metallic surface [10,26,27]. These effect of such layer on the corrosion rate is therefore limited.

Moreover, the effect of cementite in ferrito-pearlitic steels at the beginning of the corrosion processes in clayey anoxic environments is still not clearly elucidated. In a study performed on a X65 carbon steel compared to pure iron in aqueous CO_2 saturated environment, 50°C and pH 5 conditions, Owen et al, [28] highlighted that galvanic current induced by $FeCO_3$ film was much lower than the one induced by $Fe_3C/FeCO_3$ layer. The presence of cementite Fe_3C was mainly responsible for galvanic interaction.

In order to enlighten the nature of the corrosion mechanisms in the first steps of the long-term corrosion process in anoxic argileous environment, we report here the second stage of a parametric study involving ferrite and ferrito-pearlitic steel coupons at high temperature and a solution reproducing the Cox pore water. The present paper considers the system after 3 months of treatment, while the first 1-month batch was already published [20]. The objective of this paper is also to present a fine description of the morphology and the nature of the CPL, especially at the nanoscale. Indeed, the 3 month experiment is a key step to enlighten the transition between carbonate and silicate phase precipitation inside the corrosion layer. This kind of study is crucial to decipher the key parameters influencing the corrosion at this transient stage and to understand the formation of longer time corrosion layers of ferritic and ferrito-pearlitic matrix [15–18,29].

Material & Method

Samples

Two metallic substrates, a ferrito-pearlitic steel (P285NH) and a pure ferrite (Armco) were prepared and corroded during three months at 120°C in a synthetic Cox porewater (Table 1) following the procedure described by Lotz et al. [20]. Composition and microstructure images, identical to Lotz et al [20], are provided in Table 2Table 2- Chemical composition of the metallic substrate used in the corrosion experiment and Figure 1 respectively. As stated previously, a pressure of 3.3 bar of CO_2 was then added ($(P_{CO_2})_{eq}$ = 0.5 bar) followed by an additional pressure of 1 bar of helium to prevent the solution from boiling.

Table 1- Chemical composition of Bure synthetic solution in equilibrium with Bure argillite at 90°C [19].

	C [mmol.L^{-1}]
Na_2SO_4	10
KCl	0.96
$CaCl_2$	10
$MgCl_2$	2.5
$SrCl_2$	0.14
NaCl	14.7
Na_2SiO_3	0.84
$NaHCO_3$	2.62

Table 2- Chemical composition of the metallic substrate used in the corrosion experiment (%)

Elements	P285NH	Armco
C	0.15	0.002
Si	0.25	0.009
Mn	1.03	0.33
S	0.001	0.019
P	0.006	0.005
Cr	0.081	-
Mo	0.021	-
Ni	0.067	-
Cu	0.073	0.03
Fe	base	Base

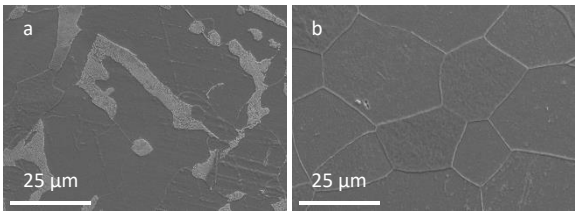

Figure 1- Scanning electron microscopy micrographs of the metallic surface after metallographic attack. (a) Ferrito-pearlitic steel P285-NH (0.15 wt.%. C) and (b) pure ferrite Armco.

Analytical techniques

Prior to analyses, samples were embedded in epoxy resin (EpoFix, Struers) and cut with a precision diamond saw (Minitom, Struers). The cross-sections were polished with SiC paper (up to grade 4000) under ethanol, and finished with 1/4 µm diamond paste on a velvet disk.

The morphology and distribution of the corrosion layers was investigated using a Field Emission Gun–Scanning Electron Microscope (JEOL SEM 7001F) operating at 10kV and equipped with Energy Dispersive X-ray spectrometer (EDS) for chemical analysis.

µ-Raman analyses were performed with a Renishaw Invia Reflex spectrometer equipped with a doubled Nd: YAG laser emitting at 532 nm and a microscope to focus the beam on the surface. Spectra were acquired between 200 and 1200 cm^{-1} at x50 magnification with a spatial resolution of 1 µm, a spectral resolution of 2 cm^{-1} and during 60 s at a power of few 100 µW.

Thin sections (~100 nm and 1 µm thicknesses) were extracted from the samples and prepared as cross sections using a Scanning Electron Microscope coupled with Focused Ga-Ion Beam FEI Nanolab 660 at CIMAP, Caen. Lamella thinning procedure is already described in the literature [20]. Preliminary observations were performed using Scanning Transmission Electron Microscopy (STEM) detector operating at 30 kV installed in the FIB-SEM. It was possible to mill different thicknesses on the same cross section, allowing to perform on the same section TEM and STXM at the Fe L-edge (100 nm) and at the Si K-edge (1 µm).

Scanning Transmission X-ray microscopy (STXM) combined with X-ray Absorption Near Edge Structure (XANES) was realised at the Fe L-edge to determine the valence state of the iron and at the Si K-edge to identify the chemical environment of the Si-rich phases. Analyses were performed at the Hermes

beamline (Fe L-edge), synchrotron SOLEIL (France) and at the 10ID-1 beamline (Fe L-edge & Si K-edge), Canadian Light Source (Canada), with equivalent beam size of about 25 nm. Data acquisition and treatment were performed with aXis2000 software following the process presented in the literature [30–32]. Iron L-edge reference spectra were acquired for this study while at the Si K-edge reference spectra came from the previously developed database [32].

Nanometric chemical and structural information was obtained using the Transmission Electron Microscope (TEM) JEOL 2010 F of IRMA (Caen) operating at 200 keV and equipped with a diode EDAX X-ray microanalysis. Phase identification were performed using Selected Area Electron Diffraction (SAED). Radial intensity profiles were obtained using the "locate selected area diffraction pattern (SADP) centre" function in manual mode and the "rotational average" function from the DiffTool package inside Digital Micrograph software [33]. Interplanar d-spacing were compared to the diffraction data d_{hkl} from the Powder Diffraction Files (PDF) database from ICDD. Phase's locations were performed through the acquisition of dark field images.

Thermodynamic modelling

The Eh/pH diagrams were drawn with the Geochemist's workbench package. The database used was the ThermoChimie_v10a developed by the consortium Andra-Ondraf/Niras-NWS [34–36]. The greigite phase was added to this database [37]. The porewater solution composition was set first according to the initial composition of the experimental solution. Although no Al species were added to the solution, a very low concentration of Al (10^{-15} mol/L) was needed to observe the b domain of silicate phases containing low levels of this element. Moreover, the carbonate concentration was estimated to about 0.01 mol/L from the initial pressure of CO_2 (following Henry's law).

Results

The CPL morphology of the ferrito-pearlitic and the ferritic sample observed on cross sections using SEM micrographs in backscattered electron (BSE) mode appeared in homogenous grey (Figure 2).

Some brighter micrometric islets appeared at the M/CPL interface as well as bright cementite lamellas for the ferrito-pearlitic sample. For the ferrito-pearlitic sample (Figure 2a), the CPL presented a discontinuous crack, parallel to the metal surface. On the contrary, the CPL of the ferritic sample (Figure 2b) appeared well adherent to the metal.

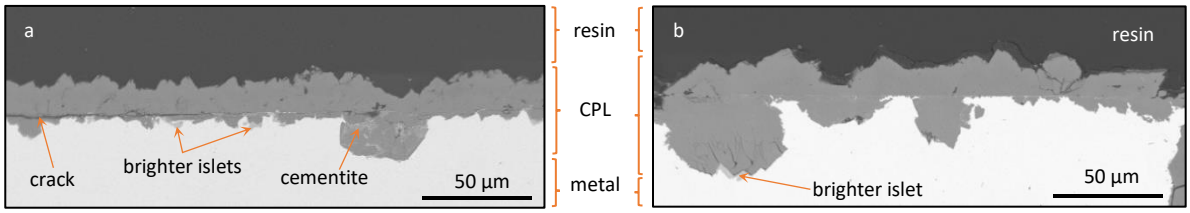

Figure 2- General morphology of (a) the ferrito-pearlitic and (b) the ferritic samples in cross section, BSE-SEM images.

CPL thicknesses measured from the metal to the resin for both samples (Figure 3) presented a similar distribution of values ranging from 6 to 62 µm and mean value of 21 and 20 µm for the ferrito-pearlitic and the ferritic samples, respectively. Compared to the previous one-month study [20], the CPL mean thickness did not change much, showing a decrease of the corrosion rate from one to three months of corrosion. Although minor, the number of localised corrosion areas showing a thickness significantly higher than the mean thicknesses, increased compared to the 1-month study and should not be overlooked. They actually constituted the main difference between the 1- and 3-month corrosion studies.

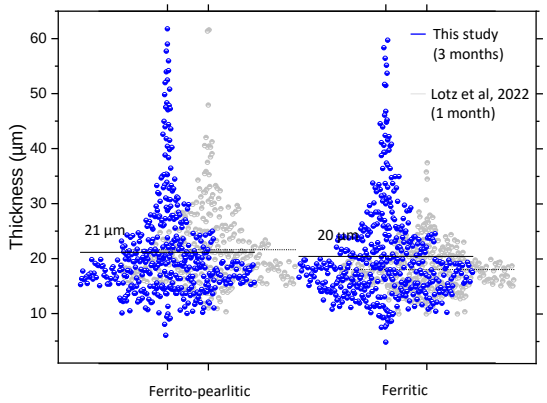

Figure 3- CPL thicknesses for the ferrito-pearlitic and the ferritic samples. The black line corresponds to the average of the measured values (ferrito-pearlitic: 421 measurements on 59 BSE-SEM images, ferritic: 431 measurements on 54 BSE-SEM images).

The spatial distribution of the elements constituting the CPL, mapped by EDS (Figure 4), evidenced a homogeneous distribution of iron and local heterogeneities at the M/CPL interface with regions containing silicon (up to 18 wt %) in the localised corrosion areas.

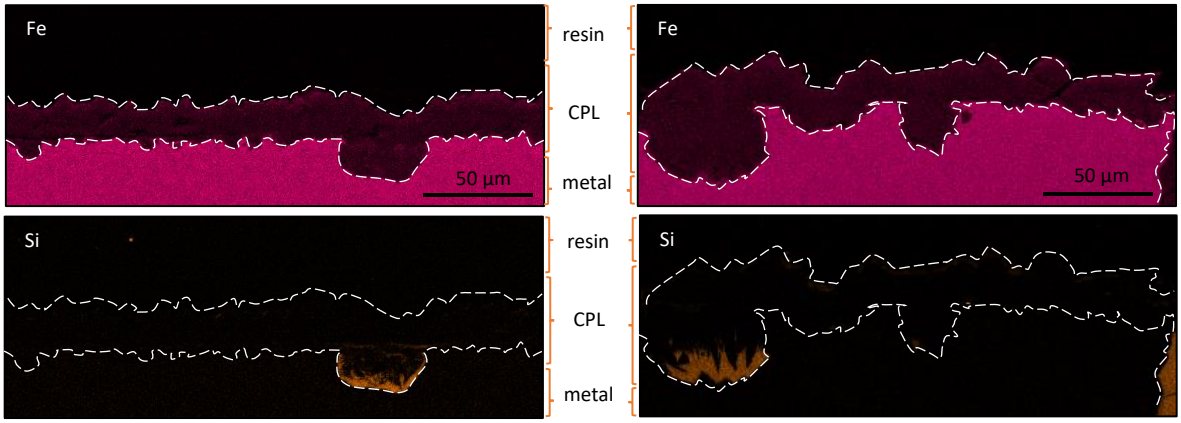

Figure 4- Spatial distribution of Fe and Si for (left) the ferrito-pearlitic and (right) the ferritic samples. EDS mapping.

The silicon-free general facies were similar to that presented by Lotz et al. [20] for a 1-month duration under the same environmental conditions.

In localised corrosion areas, associated to the presence of silicon at the M/CPL interface, the corrosion product morphology was observed with SEM micrographs in BSE mode (Figure 5).

The corrosion product appeared mostly homogenous. In addition, brighter submicrometric islets were visible in this grey matrix and at the M/CPL interface. At the interface with the metal substrate, the corrosion products appeared in slightly darker grey and cracked. Moreover, for the ferrito-pearlitic sample, cementite lamellas, embedded in the corrosion products also appeared brigher than the main matrix in the internal part of the corrosion products. As they were initially present in the metallic substrate as constituent of pearlite, they gave information on the location of the original surface of the metallic substrate. For the ferritic sample, which does not contain any cementite, morphological similarities with the one month experiment [20] allowed locating the original surface thanks to the presence of small and bright islets arranged as strips. Phases situated outer the original surface are defined in the following as external corrosion products (eCP) while phases above the original surface are called internal corrosion products (iCP).

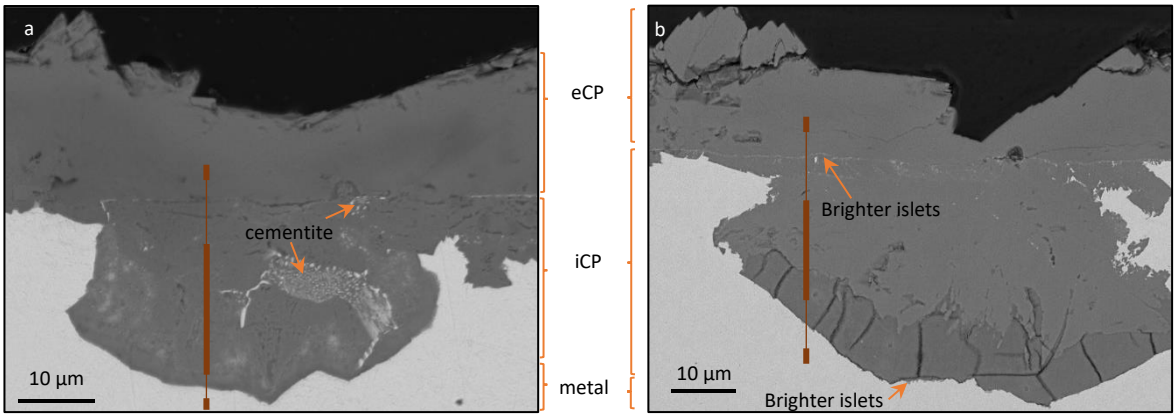

Figure 5- Observation in cross section of localised corrosion areas of (a) the ferrito-pearlitic and (b) the ferritic samples. BSE-SEM images. The brown lines correspond to the location of thin foil extractions, with 100 nm (thin line) and 1 µm (thick line) thinnings.

Chemical spatial distribution acquired by EDS (Figure 6) showed, for both samples, differences in composition in the iCP according to the morphological observations. At the M/CPL interface, a layer with thickness ranging from 4 to 30 µm contained iron, oxygen, silicon (45, 35, 18 wt. % respectively), which was homogeneously distributed. Sulphur was also detected in this interface, from 0.5 to 1 wt. % for the ferritic sample while it reached 3 wt. % locally for the ferrito-pearlitic sample. For both samples, calcium was absent from this region.

The rest of the CPL had a homogeneous distribution of oxygen with variations in iron and calcium. The proportions of iron and calcium appeared anti-correlated: the Ca-depleted and -enriched zones have the following composition: 57 wt. % Fe, 5 wt. % Ca and 46 wt. % Fe, 11 wt. % Ca, respectively. For the ferrito-pearlitic sample, silicon distribution was also heterogeneous on the iCP region containing Ca at levels about 1 to 3 wt.%. Finally, for both samples, silicon and sulphur were also evidence, although weakly, at the iCP/eCP interfaces.

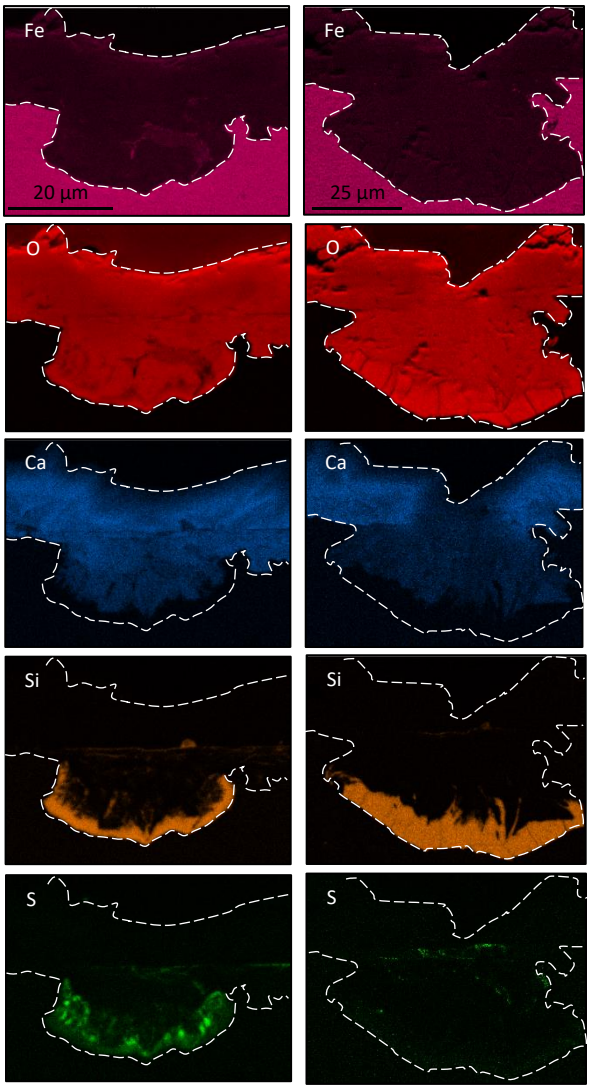

Figure 6- Spatial distribution of Fe, O, Ca, Si and S for (left) the ferrito-pearlitic and (right) the ferritic samples. EDX mapping.

Micro-Raman spectroscopy investigations in the homogeneous matrix of corrosion products containing iron, oxygen and calcium showed carbonate bands characteristic of Ca-rich siderite, throughout the CPL (Figure 7a). S-rich regions were characterised on the ferrito-pearlitic sample (Figure 7b): Raman spectra evidenced a mixture of iron sulphide, mackinawite (FeS) and greigite (Fe_3S_4) [38]. Finally, on brighter islet located at the M/CPL interface, bands at 553 and 675 cm^{-1} with medium and strong intensity respectively, highlighted the presence of magnetite [39] (Figure 7c). Lastly, the iron silicate layer exhibited a Raman spectrum obstructed by a phenomenon of fluorescence impeding the identification of the mineral phase by this technique.

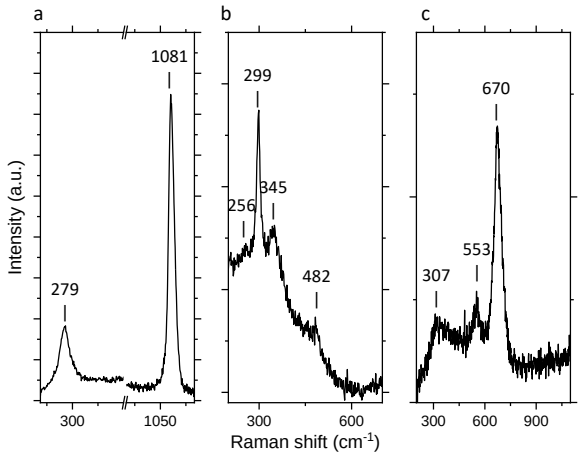

Figure 7- Representative Raman spectra acquired on (a) the carbonate layers, (b) the S-rich islets containing mackinawite and greigite and (c) magnetite brighter islets at the M/CPL interface on the localised corrosion areas.

The characterization of FIB electron-transparent lamella was pursued at the nanoscale by STEM, TEM and STXM/XANES. Solid lines on the cross-section in Figure 5 indicate the locations of thin foil extractions: thin lines for 100 nm films and large ones for 1 µm films. Figure 8a and 8b correspond to the M/CPL interface containing the silicon rich region for the ferrito-pearlitic and the ferritic samples respectively. Each image evidenced a thin brighter layer ranging from 100 nm to 4 µm at the interface between the metal and the high Si layer.

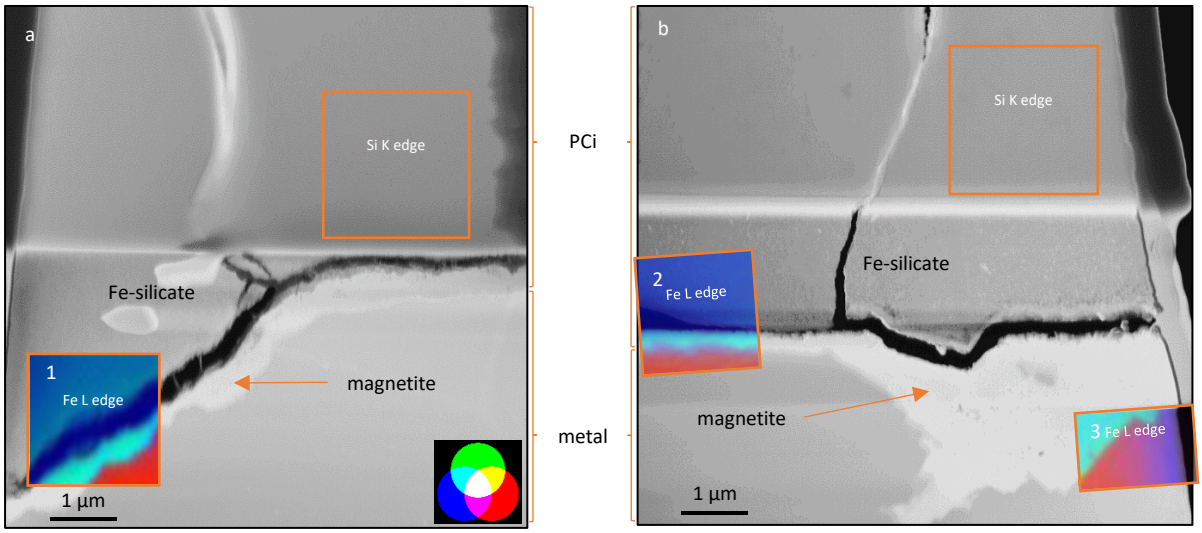

Figure 8- STEM observations of FIB lamella extracted from the local corrosion advances of (a) the ferrito-pearlitic and (b) the ferritic samples. Thinning performed at the M/CPL interface. Inserts are distribution maps of the three components Fe^{0} (red), Fe^{II} (blue) and Fe^{III} (green) acquired by STXM/XANES.

High-resolution TEM micrographs on regions containing silicon are presented in Figure 9. For both samples, results reveal disorganized foliated aggregates, compatible with the morphology of phyllosilicate particles [40].

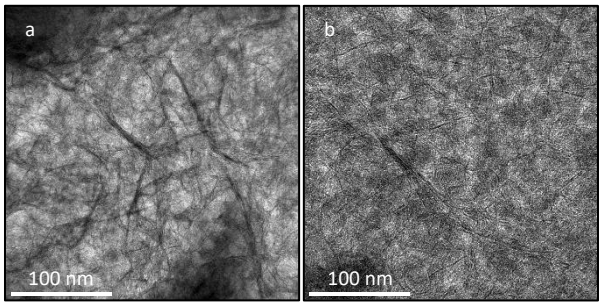

Figure 9- Morphology of the iron silicate at nanoscale acquired on (a) the ferrito-pearlitic and (b) the ferritic sample, HR-TEM.

To assess local chemical information on the Fe-Si-O rich phases, and to refine the Si-rich phases identification, STXM spectra were collected at the Si K-edge on the 1 µm thick part of FIB lamellas (Figure 10a). For both samples, experimental spectra presented a main peak at 1846.0 eV (peak A), an oscillation at 1856.3 eV (C) and an additional broad band at 1862.6 eV (D).

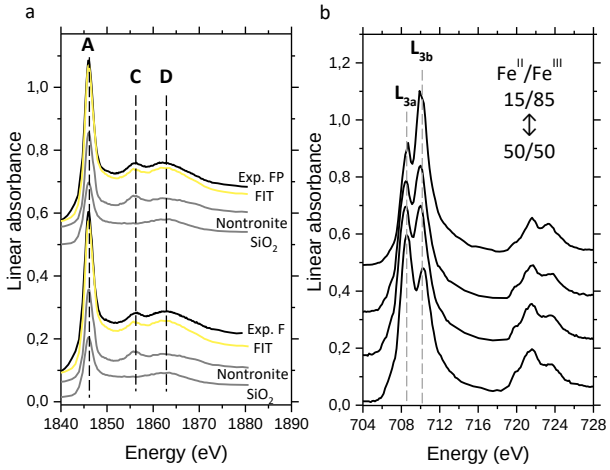

Figure 10- (a) Experimental spectra (black) acquired at Si K-edge on the silicate layer, with fit (yellow) and associate reference spectra (grey) for the ferrito-pearlitic FP and the ferritic F sample. (b) Experimental spectra (black) acquired at Fe L-edge on both samples with Fe^{II}/Fe^{III} ratio, STXM/XANES.

These two experimental spectra were decomposed by a linear regression using reference spectra of selected minerals [32]. The best fits (R^2 = 0.99 and χ^2 = 0.01) were obtained with the combination of only two reference phases: 85 % of nontronite ($Na_{0,4}Fe^{III}_2(Si, Al)_4O_{10}(OH)_2$), and 15 % of amorphous SiO_2. Note that the chemical composition was not completely consistent with the nontronite phase by

the absence of Al and Na elements. Iron L-edge spectra from the Fe-O-Si phase (Figure 10b) showed different intensities of the L_{3a} and L_{3b} peaks, which are respectively characteristic of Fe^{II} and Fe^{III} from the $2p_{3/2} \rightarrow 3d$ transition [41]. Spectra were decomposed using a linear regression with two components, one for each iron oxidation state: siderite (Fe^{II}) and maghemite (Fe^{III}). Results evidenced Fe^{II}/Fe^{III} ratio ranging from 15/85 to 50/50. Thus, considering the set of reference data to model the Si K edge, STXM results suggest the presence of a smectite with Si structural organization similar to nontronite with variable proportion of Fe^{II} and Fe^{III}. TEM observation could not confirm this hypothesis because no regular inter-reticular planes could be acquired.

Between the iron silicate layer and the metal, STEM micrographs in HAADF highlighted a brighter continuous layer at the M/CPL interface, where magnetite was identified locally by Raman spectroscopy at the microscale. The iron oxidation state was investigated by STXM/XANES in the interfacial layer observed between the metal and the silicate layer already seen by STEM. Results, treated using a singular value decomposition (SVD) with three reference spectra (Fe^0 metal, Fe^{II} siderite, Fe^{III} maghemite), are displayed in the form of RGB representations (Figure 8). For both samples, this layer appeared in cyan, indicating a mixture of Fe^{II} (blue) and Fe^{III} (green) compatible with magnetite. Linear regression performed on the cluster characteristic of this layer confirmed the presence of Fe^{II}/Fe^{III} mixture in a 1:2 ratio, close to the one of magnetite (Fe^0 was added to the fit because of the layer proximity with the metallic part)[32].

Figure 11 corresponds to the STEM observation in HAADF mode of the FIB lamella extracted from the part of the layer containing iron carbonate. On each image, the iCP/eCP interface was well observed and indicated with orange dashes on the images. Although siderite was present on both sides of the interface, the matrix presented differences in density and porosity.

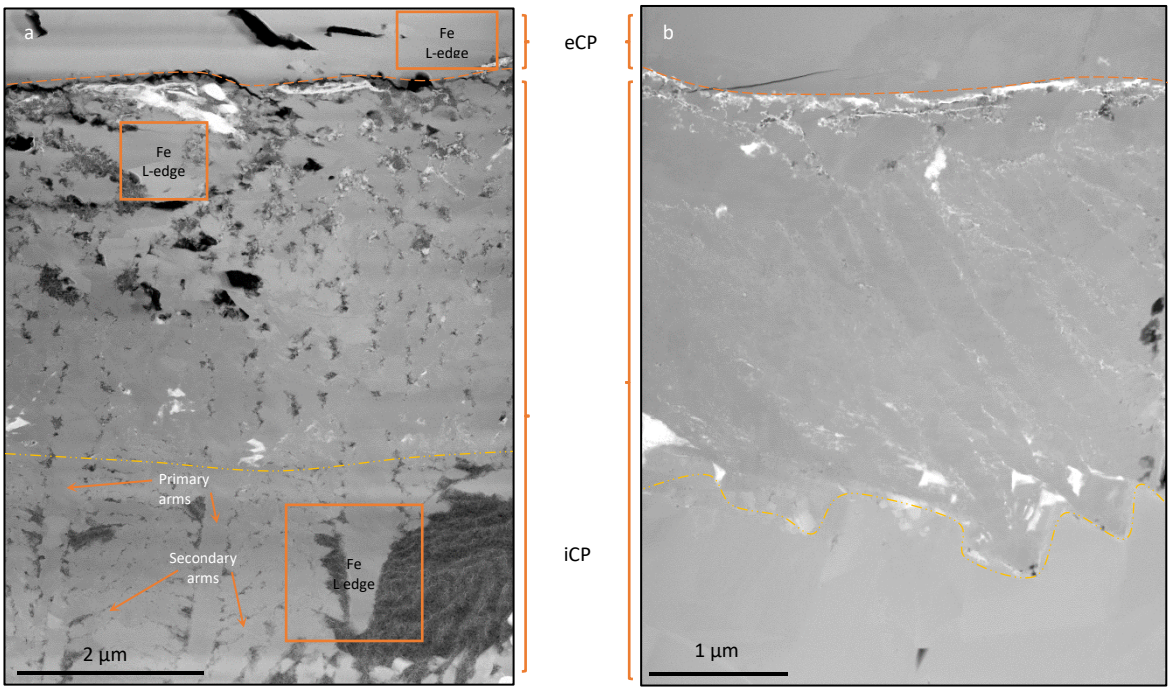

Figure 11- Observations of thin sections taken from the localised corrosion areas of (a) the ferrito-pearlitic and (b) the ferritic samples. Thinning performed around the sample original surface delimited with yellow dashes. Yellow dot lines delimit two carbonate layers with different morphologies, STEM HAADF.

The eCP was rather homogeneous in both samples, but the carbonate in the iCP differed from that in the eCP. It presented two zones, named outer and inner iCP in the following, which were themselves distinguished by their morphology (delimited with yellow dashes). Although outer and inner iCP were observed on both samples their characteristics differed from one sample to another. For the ferrito-pearlitic sample (Figure 11a), the outer iCP contained porosities of various size, from 10 to 300 nm and some brighter nanometric islets. This morphology was also observed from the 1-month study and the generalized corrosion facies of this 3-month study. In addition, the inner iCP presented specific morphology, suggesting precipitation from a solution. The interstitial porosity induced by these precipitated crystals appeared filled by a less dense phase analysed by TEM-WSD. This phase contained up to 14 wt. % of Si with morphology typical of iron silicate [40]. Distinctively, for the ferritic sample (Figure 11b), the outer iCP presented bright nanometric filaments and local porosity while the inner iCP appeared homogeneous and similar to the eCP.

In order to investigate any structural differences between these three carbonate areas of the eCP and outer and inner iCP, Raman, TEM/SAED and STXM/XANES at Fe L-edge were performed (Figure 12).

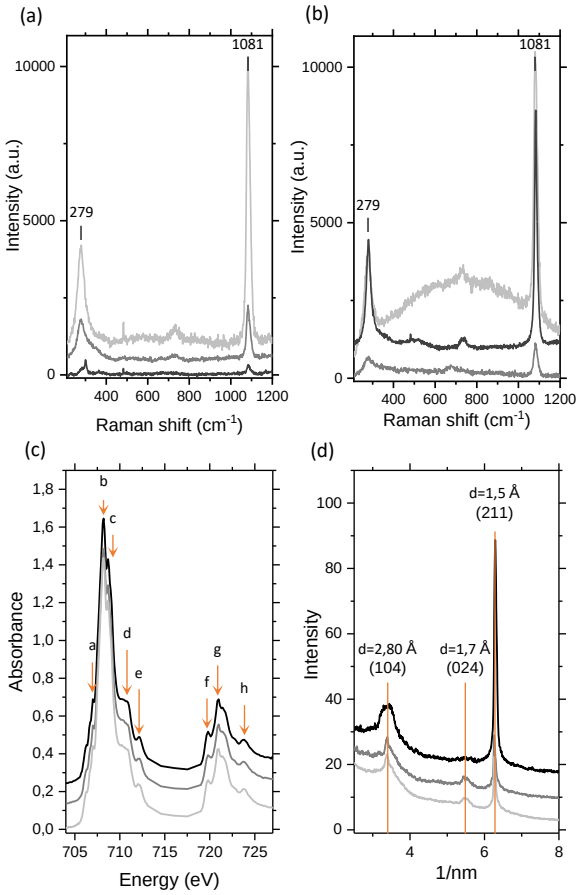

Figure 12- (a-b) Raman spectra characteristic of the carbonate structure acquired on each region for the ferrito-pearlitic and the ferritic steel respectively. (c) Experimental Fe L-edge spectra acquired on carbonate regions of the ferrito-pearlitic sample, typical from siderite. (d) Radially integrated diffraction data from diffraction pattern acquired on the carbonate region of the ferritic sample. Legend: black; eCP, dark grey; outer iCP, light grey; inner iCP.

Raman analysis performed on the three areas of both samples evidenced bands at 280 and 1080 cm^{-1} confirming the presence of the carbonate group of siderite (Figure 12a and b). The iron carbonate spectra exhibited differences, depending on their localisation in the CPs, in the carbonate peak intensities, suggesting that the crystalline nature (e.g., crystal orientation, the degree of crystallinity and/or the grain size of the crystallites) of these carbonates varied [42]. STXM/XANES analyses were acquired on the ferrito-pearlitic sample (Figure 12c) while TEM/SAED (Figure 12d) were acquired on the ferritic sample. Absorption spectra acquired by STXM/XANES on each region of the ferrito-pearlitic sample (on Figure 12c) evidenced the similar bands and shapes, typical of Fe(II) in a C_{3v} distorted octahedral symmetry, such as siderite [43,44]. In addition, radially integrated electron diffraction patterns acquired by SAED on the ferritic sample (Figure 12d) for the three areas, presented d-spacings

compatible with siderite. Thus, the micro- to nanoscale characterization results was the same for the three regions, although they present various morphologies suggesting different precipitation mode.

The presence of iron oxide in this carbonate region was also investigated. Dark field images were acquired by positioning the objective aperture on the d-spacing of 2.9 Å of magnetite-maghemite pattern. Consequently, all the crystallites with the same orientation as the diffracted crystallite appeared brighter in the dark field images on Figure 13. For both samples, nanometric islets (0.02 - 0.05 µm) appeared brighter in the iCP outer part. For the ferritic sample, these islets seemed to form an interconnected network.

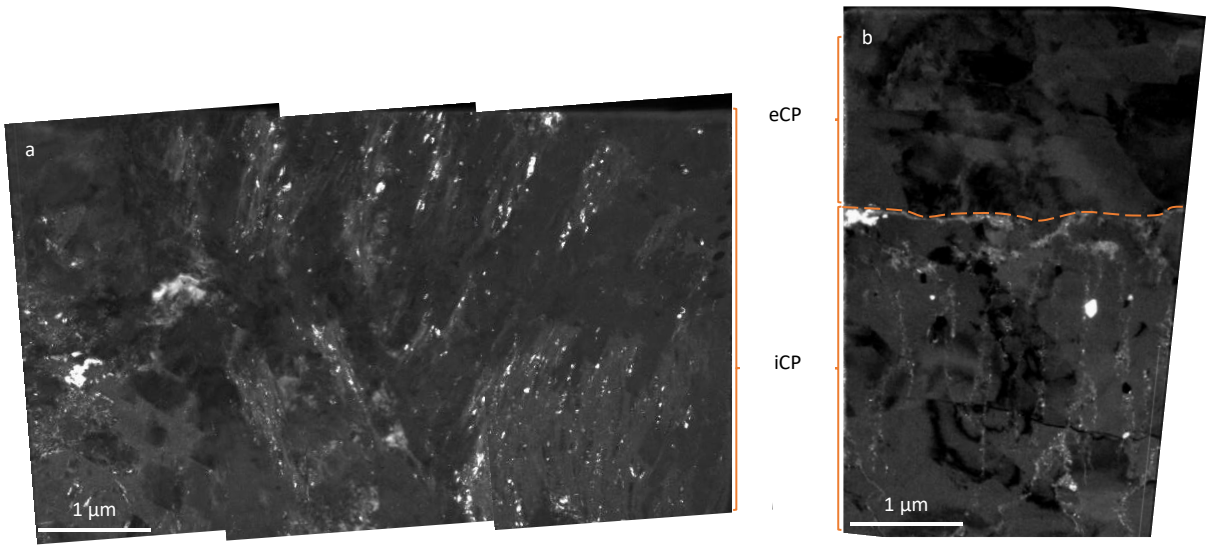

Figure 13- Location of nanometric to micrometric oxide islets the localised corrosion facies of (a) the ferrito-pearlitic and (b) the ferritic samples. Dark field TEM orientation images obtained by positioning the aperture of the objective on a magnetite diffraction spot.

Discussion

The investigation of iron and steel corroded at 120°C during 3 months provides further information on the evolution of the morphology and nature of the corrosion facies compared to the one-month study [20]. A schematic representation of the corrosion facies at 3 months is presented in Figure 14.

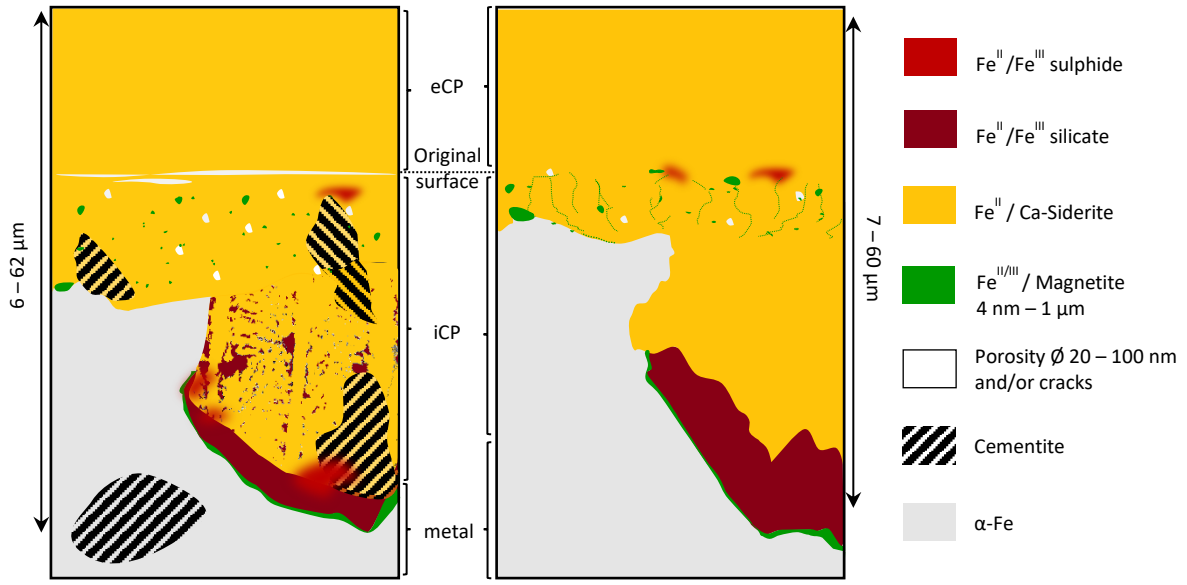

Figure 14- Schematic representation of the corrosion facies with localised corrosion for ferrito-pearlitic (left) and ferritic (right) samples.

The main part of the corrosion facies (on the left of each schematic representations), was in all aspects identical to the one observed after one month of corrosion [16], with the presence of a Ca-siderite bilayer which interface indicated the location of the former original surface of the metal.

The precipitation of an iron carbonate layer has been widely studied. Depending on the precipitation condition of siderite, the layer can have an effect on the corrosion rate [1]. The presence of a dense and poorly porous $FeCO_3$ layer reduces mass transport which lead to a decrease of the corrosion rate. As characterized by Lotz et al after one month in Cox porewater [20], these environmental conditions seem to favour the precipitation of a carbonate layer that will act as a diffusion barrier (temperature of 120°C and 400 ppm of Ca^{2+} in solution). After 3 months in the same conditions, the average corrosion layer thickness is very close for both experiments consolidating this observation. The impact on the corrosion rate will be discussed later in this discussion.

The bi-layer structure was also observed by Gao et al. [45] and De Motte et al. [24] on steel corroded in carbonated environment as well as by Schlegel et al. [17] on steel corroded in compact clay environment containing a porewater similar to our study. The latter also located the original surface of the sample between two layers of Ca-siderite in the case of a ferrito-pearlitic sample, based on the

presence of cementite lamellas detected only in the CPL. In addition, nanometric magnetite islets were observed in the iCP and nano to micrometric magnetite islets at the M/CPL interface [46,1]. This facies is typical of iron corrosion in carbonated environment [1,24]. However, the comparison between the ferrito-pearlitic and the ferritic samples highlighted a difference in the morphology of the iCP. It is more porous for the ferrito-pearlitic sample and this could be explained by a possible decoupling of the anodic and cathodic reaction in the whole iCP in the presence of conducting cementite connecting electrically the metal to the bilayer (iCP/eCP) interface. This part of the corrosion system will not be discussed further here and a detailed consideration of the mechanism can be found elsewhere [20,47].

After 3-month exposure, both samples presented localised corrosion areas with a significantly higher thickness and made of Ca-siderite, iron silicate, magnetite as well as locally iron sulphide as greigite and mackinawite. The localised corrosion areas appeared to grow under the initial Ca-siderite bi-layer (bright yellow on Figure 14). This initial bi-layer was still constituted of the eCP outer the original surface and the iCP below the original surface.

Morphology, nature and phase distribution of these localised corrosion areas shared common features with corrosion products observed by other studies performed on iron and steel corroded in contact with compact clay [15–18] and Cox porewater [48], in the presence of carbonate and silicate species, at 90°C for 7 to 76 months. Nevertheless, in these previous studies, these characteristics were generalized. However, the localised corrosion areas observed here were far from reaching the general corrosion facies presented on the literature. This is likely due to the treatment duration of the present study (3 months) which was significantly shorter than the one of previous studies. Moreover, the presence of the localised corrosion areas did not have a significant impact on the CPL thickness average for both steel and ferrito-pearlitic samples between 1 and 3 months of experiment [20]. The negligible evolution of the CPL thickness suggested that the general facies made of the carbonate bi-layer acted on the corrosion rate, probably as a diffusion barrier to electrochemically active species to reach anodic sites [49].

In addition, in the localised corrosion areas, morphological changes of the carbonate matrix at the vicinity of the metallic substrate suggested the development of an additional Ca-siderite layer in the inner part of the iCP (dark yellow on Figure 14). At this location, in both samples, the distinct morphology between the outer and the inner parts of the iCP (Figure 11) suggests some local changes in the corrosion condition, although the local conditions were still in favour of carbonate precipitation. Moreover, the different siderite morphologies at this location between the ferrito-pearlitic and the ferritic samples, i.e. precipitated isolated siderite crystals with porous or dense layer respectively, highlighted different mode of Ca-siderite precipitation that could be related to the different metal microstructure. To our knowledge such local changes in the inner part of the Ca-siderite has not been reported in the literature. The formation of siderite includes a nucleation-growth process related to supersaturation [1]. The porous morphology of the siderite layer for the ferrito-pearlitic sample suggested a process controlled by nucleation, which indicated a high supersaturation ratio during the precipitation of this layer. The presence of cementite lamellas might have reduced the mass transport processes between the environmental and porewater solutions. Either cementite acts as a diffusion barrier, leading to a local accumulation of Fe^{2+} cations and/or CO_3^{2-} anions, or as additional cathodic reaction sites to accelerate corrosion, which will increase locally Fe^{2+} concentration as stated in the literature [28]. On the contrary, the siderite inner iCP morphology of the ferritic sample suggested a process dominated by crystal growth, which is related to a low level of supersaturation. Thus, the difference between the ferrito-pearlitic and the ferritic samples might be related to differences in the supersaturation level in the CPL porewater, and thus to differences in the porewater chemistry ($[Fe^{2+}]$ and $[CO_3^{2-}]$), as well as the growth of siderite grains on different surfaces (metal and cementite for the ferrito-pearlitic sample and metal only for the ferritic one). It can be questioned whether the presence of cementite could affect the growth process of the siderite grains and favour their nucleation in the outer part of the iCP layer of the ferrito-pearlitic sample, inducing the formation of porosity.

The presence of iron silicate and iron sulphide more internally in the localised corrosion areas and of a magnetite layer at the M/CPL interface, confirms the trend of local chemical conditions on these

layers, precipitated at the latest. For the ferrito-pearlitic sample, the iron silicate also fills the porosity of the Ca-siderite suggesting a slight change of chemical conditions locally in the porosity (see thermodynamic consideration below).

The 3-months experiment facies show an intermediate state between the one-month experiment [20] and the experiments performed during longer duration in similar conditions [15,17,29,50]. Indeed, the corrosion system observed in the local corrosion areas after 3 months seemed to be generalised and to become uniform in longer duration experiments where the silicate phase was observed along the whole M/CPL interface. As present corrosion experiments were performed in confined environment, a first hypothesis for such a modification of the corrosion process might be linked to a decrease of the carbonate ion concentration in the porewater of the localized corrosion areas. After a given duration, between 1 and 3 months, the solubility limit of siderite might not be reached anymore and led to the precipitation of other species. Another hypothesis for explaining such an evolution of the corrosion product nature might be related to a local evolution to a more basic pH which favoured the precipitation of iron silicate, sulphide and oxide species. The Eh/pH diagrams of the Figure 15 were calculated with a Cox solution at 120°C by selecting the phases identified in this study. The iron silicate chosen was the Na-Nontronite phase which should be close to the identified silicate. Figure 15a presents the diagram corresponding to the initial chemical composition of the solution, with a $[H_4SiO_4]/[CO_3^{2-}]$ ratio of 0.1, while Figure 15b,e and Figure 15c,f corresponds to an increase of this ratio to 1 and 10, respectively, by decreasing $[CO_3^{2-}]$ and simulating the hypothesis of the carbonate consumption in the interstitial solution of corrosion layer pores. Two series of diagrams were calculated: the first with the thermodynamic data of the greigite and mackinawite, for which only the greigite domain appears and the second by suppressing the greigite data allowing the mackinawite domain to appear. Results showed that both iron sulphides present superimposed predominance domains.

The diagrams illustrate the hypothesis of a local chemical evolution of the solution inside the pores of the corrosion layer by showing the different predominance domain of the phases identified in this study and their evolution. First, by deaeration of the solution at a close to neutral pH, siderite is favoured. Magnetite can be predominant while pH increases slightly for a strong decrease of the carbonate concentration. This thermodynamic simulation shows that whatever the silicate/carbonate ratio is, the predominance domain of the silicate and carbonate phases does not significantly change. Thus, the iron silicate growth in the inner part of the corrosion products seems rather to result from an increase of the pH at this location. Some authors propose a local increase of the pH due to a local increase of OH^- concentration and a low replenishment in H^+ that could be consumed by the cathodic reaction [46,51–53].

$$2H_2O + e^- \rightarrow H_2 + 2HO^- \quad (1)$$

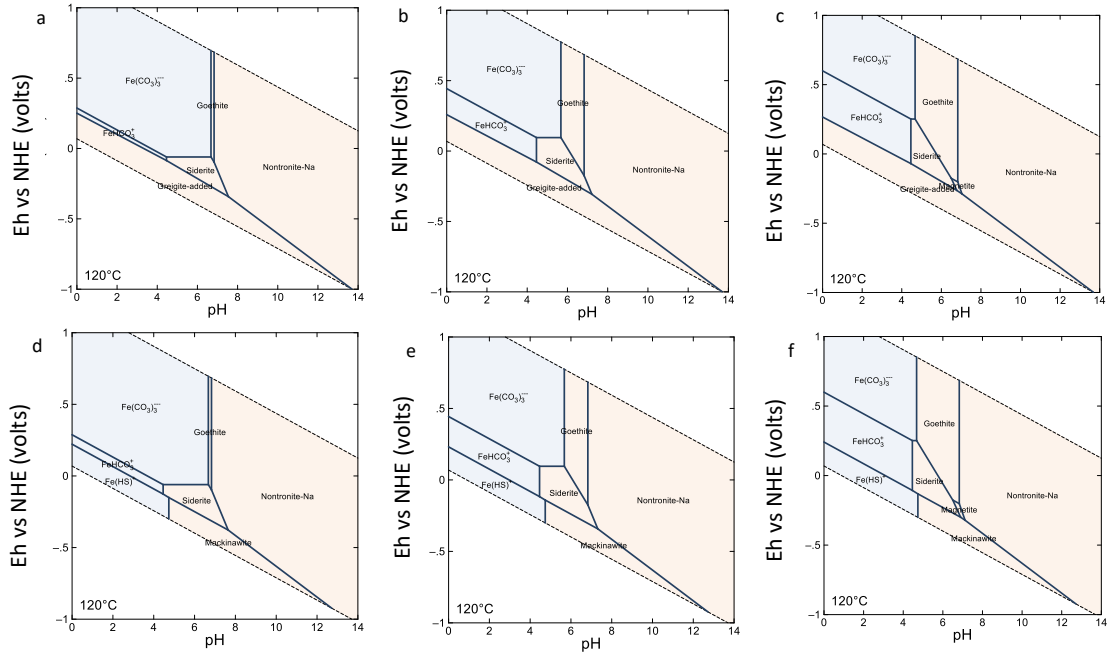

Figure 15- Eh (NHE)/pH diagram calculated with the solution concentration, [Fe^{2+}]=0.1 mmol/L, , [H_4SiO_4] = 0.1 mmol/L, [SO_4^{2-}] = 0.01 mol/L, [Al^{3+}] = 10^{-15} mmol/L, [Ca^{2+}] = 10^{-2} mmol/L, [Cl^-] = 20 mmol/L, [Na^+] = 20 mmol/L, [Sr^{2+}] = 0.1 mmol/L, [K^+] = 1 mmol/L, (a&d) [CO_3^{2-}] = 10 mmol/L, (b&e) [CO_3^{2-}] = 1 mmol/L, (c&f) [CO_3^{2-}] = 0.1 mmol/L. a,b, c were calculated using greigite while d, e, f were calculated using mackinawite

The thin continuous interfacial layer of magnetite between the metal and the iron silicate layer was observed in other similar systems, but after longer treatment durations [22,51,54]. Interestingly, in a study performed at 120°C in a Cox porewater solution, with no carbonate species in the environment and with higher Si content, the formation of a magnetite layer seemed favoured at the interface

between the metal and the CPL made of iron silicate [26]. Similar experiments performed at 50°C in deaerated solutions on iron powder with different Si species concentration in the environment confirmed the precipitation of iron oxide concurrently with iron silicate around metallic particles [27]. As for the silicate-carbonate system previously evocated, it can be suggested that the local high pH condition might also favour the formation of magnetite at the M/CPL interface [46,51–53].

Once formed, this magnetite layer is assumed to control the kinetics of the corrosion mechanism. Modelling studies [21] described a passive layer made of iron oxide that was supposed to form by a solid-state process at the metal/corrosion product interface and to dissolve at the outer interface forming another corrosion products (in our case iron silicate, iron carbonate, iron sulphide). This hypothesis is plausible for the ferritic sample for which anodic and cathodic reactions should be both located at the metal/corrosion product interface. In the case of decoupling of these reactions for the ferrito-pearlitic sample, the kinetic control could be more complex in presence of connected conductive phases as cementite and/or magnetite in the corrosion layers.

The precipitation of a dense layer of iron silicate might be related to the presence of iron carbonate. As previously reported [26,27], in a strictly silicate environment, the precipitated iron silicates were poorly adherent to the metallic substrate and appeared porous. In our experiment; cracks probably being induced by sample drying after the experiment, the iron silicate layer nevertheless appeared compact between the metallic sample and the carbonate layers. One hypothesis is that the presence of a dense layer of iron carbonate created a confined environment for iron silicate to precipitate and led to the formation of this dense layer of iron silicate. If an iron silicate such as nontronite (smectite group) precipitated, it could have a swelling behaviour [6]. Thus, they might act in the diffusion process by retaining cation.

Finally, the presence of iron sulphide was identified mainly in the silicate layer and sometimes in the siderite areas of the iCP. The absence of iron sulphide in the Ca-siderite bi-layer after the 1-month

experiment [20] and its presence only in the localised corrosion areas of the iCP after 3 months of corrosion suggested that iron sulphide precipitated after the development of the carbonate bi-layer.

Iron sulphides were already reported in other studies involving iron/clay interface [17]. However, the possible source of S in these studies was multiple: porewater, pyrite from the clay, sulphate-reducing prokaryotes. In our study, the only possible source of S was Na_2SO_4 from the porewater, in absence of bacteria in the experiment. It is assumed that iron sulphide comes from the reduction of sulphate of the porewater due to S accumulation in the CPL on the cathodic sites. Thus, iron sulphides could be indicative of the presence of cathodic site and local reducing condition inside the CPL as also suggested by the Pourbaix diagram of Figure 15 [55].

In addition, the iron sulphides greigite and mackinawite proved that locally, inside the iCP where silicate precipitated, the redox potential could have decreased and favoured the precipitation of sulphide phases. Mackinawite can precipitate and induce an increase of pH according to [56] following the reaction

$$4Fe + SO_4^{2-} + 3HCO_3^- + 5H^+ \rightarrow FeS + 3FeCO_3 + 4H_2O \quad (2)$$

Moreover, greigite can be obtained by the oxidation of the mackinawite according to [57] following the equations

$$4FeS + 2H_2O \rightarrow Fe_3S_4 + Fe(OH)_2 + H_2 \quad (3)$$

Or, according to [58]

$$3FeS + H_2S \rightarrow Fe_3S_4 + H_2 \quad (4)$$

Whatever the reaction pathway, greigite stems from mackinawite and its presence together with mackinawite inside the iCP denotes the ongoing processes of the formation of the iron sulphides. Sherar et al [59] demonstrated that the presence of iron sulphide can destabilize iron oxides formed on the metallic surface and increase the corrosion rate by creating a galvanic loop between S-rich CPL areas (anode) and S-free CPL areas (cathode) [60]. In the case of the 3-month experiments presented

in this study, the impact of the sulphide phases on the corrosion rate can be questioned due to their local precipitation at a micrometric scale inside the silicate layer. This should depend on their connexion to the metallic matrix which could, in this case increase the surface for the cathodic reaction.

Interestingly, iron sulphides appeared more present in the ferrito-pearlitic steel CPL than in the ferritic steel. This might be related to the presence of cementite in the iCP. Thanks to its conductive properties [61], cementite could act as cathodic sites for the reduction of sulphate ions.

To conclude the discussion on the corrosion kinetics, the average corrosion rates of the various experiments performed in carbonate environment within a short period of time between 75°C and 120°C [20,45,62,63] and at longer duration of several months to years in argillite media at 90°C [15,19] are reported in Figure 16. First, comparison with the average corrosion rate obtained at 120°C after few days in carbonate environment and after 1 month in Cox porewater shows that the values obtained in this study after 3 months are part of a decreasing trend of the corrosion rate at this temperature. This can be explained by the siderite growth acting as a diffusion barrier for the corroding species even though a role of the oxide nano- to micro-layer detected at the interface cannot be excluded. Second, it can be observed that at longer duration the average corrosion rate stabilises around several µm per year for all kind of substrate and conditions. Whatever the nature of the anoxic carbonated environment, the corrosion mitigation is of the same order of magnitude after several years, probably due to the combined effect of the different phases on the diffusion of species. However, a slight difference is observed between the ferritic and ferrito-pearlitic substrates after longer duration than one year in argillite conditions at 90°C. It can be questioned whether the presence of conductive cementite still in contact with the metal maintains a higher corrosion rate for the ferrito-pearlitic substrates than for the ferritic ones for which the corrosion layer might constitute an insulating barrier between the metal and the medium.

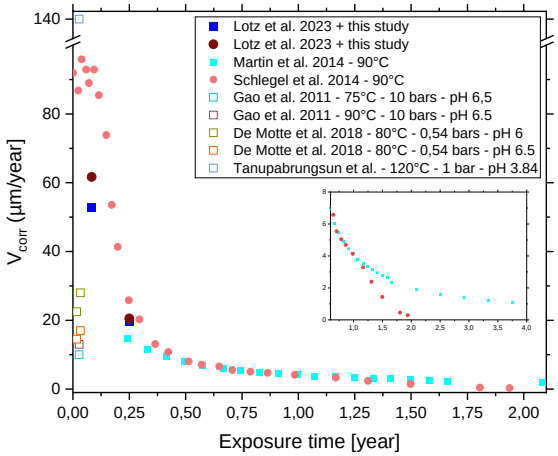

Figure 16- Average corrosion rate measured in this study and compared with various other experimental studies. Squares: Ferrito-perlitic steel, dots: ferritic steel. Empty signs: carbonate environment, filled signs: carbonate/silicate environment.

Conclusion

This study provides new insights into the understanding of the evolution of the morphology and nature of the corrosion product layers of a ferrito-pearlitic steel and a ferritic steel in the presence of Cox porewater. The corrosion duration of 3 months is intermediate between very short exposure times and longer ones already published.

For both metallic substrates, the weak evolution of the average CPL thickness from one to three months confirms the Ca-siderite bi-layer acts as a diffusion barrier.

The very first step of generalized corrosion, after 1 month treatment, produced a Ca-siderite bi-layer. But, after 3 months, localized corrosion areas begin to form with a thickness significantly higher than the average thickness of the Ca-siderite bi-layer. They are constituted of (i) iron carbonate, (ii) iron silicate, (iii) iron sulphide and (iv) iron oxide. The transition from a carbonate system to a mixed system suggests the porewater chemistry changes locally, probably due to a reduction of the carbonate concentration in solution and/or to a pH increase. The effect of the metal microstructure seems to rely on the morphology of the iCP carbonate layers and especially in the localised corrosion areas, the location of Fe-Si-O phases and the amount of iron sulphide on the CPL. The presence of a continuous

layer of magnetite between the metal and the iron silicate layer might be the onset of the formation of a passive layer controlling the corrosion rate. This specific facies seems to be transient and to tend to a more generalised corrosion facies for longer durations (i.e. years).

Declaration of Competing Interest

The authors declare that they have no known competing financial interests or personal relationships that could have appeared to influence the work reported in this paper.

Data Availability

The data that support the findings of this study are available from the corresponding author upon reasonable request.

Acknowledgments

This study was partially supported by the ANR funding "Investissements d'avenir" ANR-11-EQPX-0020 (Equipex GENESIS), by the Fonds Européen de Developpement Régional, and by the Région Basse-Normandie. The Canadian Light Source is supported by NSERC, CIHR, NRC, the Province of Saskatchewan, WEDC, and the University of Saskatchewan. Authors thank the Hermes team at SOLEIL; Rachid Belkhou, Stefan Stanescu and Sufal Swaraj; for the beamtime and their help during the experiment.

References

[1] R. Barker, D. Burkle, T. Charpentier, H. Thompson, A. Neville, A review of iron carbonate (FeCO3) formation in the oil and gas industry, Corrosion Science. 142 (2018) 312–341. https://doi.org/10.1016/j.corsci.2018.07.021.

[2] H. Matthiesen, L.R. Hilbert, D. Gregory, B. Sørensen, Corrosion of archaeological iron artefacts compared to modern iron at the waterlogged site Nydam, Denmark., in: Nice, 2004: p. 12.

[3] D. Féron, D.D. Macdonald, Prediction of Long Term Corrosion Behaviour in Nuclear Waste Systems, MRS Proc. 932 (2006) 35.1. https://doi.org/10.1557/PROC-932-35.1.

[4] N.R. Smart, The Corrosion Behavior Of Carbon Steel Radioactive Waste Packages: A Summary Review Of Swedish And U.K. Research, in: 2008: p. NACE-P3013.

[5] D. Féron, D. Crusset, J.-M. Gras, Corrosion issues in nuclear waste disposal, Journal of Nuclear Materials. 379 (2008) 16–23. https://doi.org/10.1016/j.jnucmat.2008.06.023.
[6] D. Crusset, Y. Linard, C. martin, N. Michau, S. Necib, S. Schumacher, synthèse et bilan des travaux du groupement de laboratoires verre - fer - argiles 2006-2014, 2015.
[7] D. Guillaume, A. Neaman, M. Athelineau, R. Mosser-Ruck, C. Peiffert, M. Abdelmoula, J. Dubessy, F. Villiéras, N. Michau, Experimental study of the transformation of smectite at 80 and 300°C in the presence of Fe oxides, Clay Miner. 39 (2004) 17–34. https://doi.org/10.1180/0009855043910117.
[8] M. Jeannin, D. Calonnec, R. Sabot, Ph. Refait, Role of a clay sediment deposit on the corrosion of carbon steel in 0.5molL−1 NaCl solutions, Corrosion Science. 52 (2010) 2026–2034. https://doi.org/10.1016/j.corsci.2010.02.033.
[9] C. Rivard, M. Pelletier, N. Michau, A. Razafitianamaharavo, I. Bihannic, M. Abdelmoula, J. Ghanbaja, F. Villieras, Berthierine-like mineral formation and stability during the interaction of kaolinite with metallic iron at 90 C under anoxic and oxic conditions, American Mineralogist. 98 (2013) 163–180. https://doi.org/10.2138/am.2013.4073.
[10] P. Le Pape, C. Rivard, M. Pelletier, I. Bihannic, R. Gley, S. Mathieu, L. Salsi, S. Migot, O. Barres, F. Villiéras, N. Michau, Action of a clay suspension on an Fe(0) surface under anoxic conditions: Characterization of neoformed minerals at the Fe(0)/solution and Fe(0)/atmosphere interfaces, Applied Geochemistry. 61 (2015) 62–71. https://doi.org/10.1016/j.apgeochem.2015.05.008.
[11] M. Saheb, D. Neff, Ph. Dillmann, H. Matthiesen, E. Foy, Long-term corrosion behaviour of low-carbon steel in anoxic environment: Characterisation of archaeological artefacts, Journal of Nuclear Materials. 379 (2008) 118–123. https://doi.org/10.1016/j.jnucmat.2008.06.019.
[12] M. Saheb, D. Neff, J. Demory, E. Foy, P. Dillmann, Characterisation of corrosion layers formed on ferrous archaeological artefacts buried in anoxic media, Corrosion Engineering, Science and Technology. 45 (2010) 381–387. https://doi.org/10.1179/147842210X12772898886889.
[13] O. Bildstein, L. Trotignon, M. Perronnet, M. Jullien, Modelling iron–clay interactions in deep geological disposal conditions, Physics and Chemistry of the Earth, Parts A/B/C. 31 (2006) 618–625. https://doi.org/10.1016/j.pce.2006.04.014.
[14] G. de Combarieu, P. Barboux, Y. Minet, Iron corrosion in Callovo–Oxfordian argilite: From experiments to thermodynamic/kinetic modelling, Physics and Chemistry of the Earth, Parts A/B/C. 32 (2007) 346–358. https://doi.org/10.1016/j.pce.2006.04.019.
[15] M.L. Schlegel, C. Bataillon, F. Brucker, C. Blanc, D. Prêt, E. Foy, M. Chorro, Corrosion of metal iron in contact with anoxic clay at 90 °C: Characterization of the corrosion products after two years of interaction, Applied Geochemistry. 51 (2014) 1–14. https://doi.org/10.1016/j.apgeochem.2014.09.002.
[16] M.L. Schlegel, M. Sennour, C. Carriere, F. Martin, M. Fenart, J. Varlet, C. Blanc, P. Dillmann, D. Neff, J.J. Dynes, Corrosion at the steel-clay interface at 90°C: nanoscale characterization of metal-replacing corrosion products, (2017).
[17] M.L. Schlegel, F. Martin, M. Fenart, C. Blanc, J. Varlet, E. Foy, D. Prêt, N. Trcera, Corrosion at the carbon steel-clay compact interface at 90°C: Insight into short- and long-term corrosion aspects, Corrosion Science. 152 (2019) 31–44. https://doi.org/10.1016/j.corsci.2019.01.027.
[18] M.L. Schlegel, F. Martin, M. Fenart, C. Blanc, J. Varlet, E. Foy, Corrosion of carbon steel in clay compact environments at 90 °C: Effect of confined conditions, Corrosion Science. 184 (2021) 109368. https://doi.org/10.1016/j.corsci.2021.109368.
[19] F. Martin, S. Perrin, M. Fenart, M. Schlegel, C. Bataillon, On corrosion of carbon steels in Callovo-Oxfordian clay: Complementary EIS, gravimetric and structural study providing insights on long term behaviour in French geological disposal conditions, Corrosion Engineering Science and Technology. 49 (2014) 460–466. https://doi.org/10.1179/1743278214Y.0000000181.
[20] H. Lotz, D. Neff, F. Mercier-Bion, C. Bataillon, P. Dillmann, E. Gardes, I. Monnet, Iron and steel corrosion mechanisms in a carbonate rich pore water: Multiscale characterization of the corrosion product layers, Materials and Corrosion. 74 (2023) 8–19. https://doi.org/10.1002/maco.202213417.

[21] C. Bataillon, F. Bouchon, C. Chainais-Hillairet, C. Desgranges, E. Hoarau, F. Martin, S. Perrin, M. Tupin, J. Talandier, Corrosion modelling of iron based alloy in nuclear waste repository, Electrochimica Acta. 55 (2010) 4451–4467. https://doi.org/10.1016/j.electacta.2010.02.087.
[22] Y. Leon, P. Dillmann, D. Neff, M.L. Schlegel, E. Foy, J.J. Dynes, Interfacial layers at a nanometre scale on iron corroded in carbonated anoxic environments, RSC Adv. 7 (2017) 20101–20115. https://doi.org/10.1039/C7RA01600J.
[23] B. Kinsella, Y.J. Tan, S. Bailey, Electrochemical Impedance Spectroscopy and Surface Characterization Techniques to Study Carbon Dioxide Corrosion Product Scales, CORROSION. 54 (1998) 835–842. https://doi.org/10.5006/1.3284803.
[24] R. De Motte, E. Basilico, R. Mingant, J. Kittel, F. Ropital, P. Combrade, S. Necib, V. Deydier, D. Crusset, S. Marcelin, A study by electrochemical impedance spectroscopy and surface analysis of corrosion product layers formed during CO2 corrosion of low alloy steel, Corrosion Science. 172 (2020) 108666. https://doi.org/10.1016/j.corsci.2020.108666.
[25] M.A. Kindi, G.R. Joshi, K. Cooper, J. Andrews, P. Arellanes-Lozada, R. Leiva-Garcia, D.L. Engelberg, O. Bikondoa, R. Lindsay, Substrate Protection with Corrosion Scales: Can We Depend on Iron Carbonate?, ACS Appl. Mater. Interfaces. 13 (2021) 58193–58200. https://doi.org/10.1021/acsami.1c18226.
[26] H. Lotz, C. Carrière, C. Bataillon, E. Gardes, I. Monnet, E. Foy, M.L. Schlegel, J.J. Dynes, D. Neff, F. Mercier-Bion, P. Dillmann, Investigation of steel corrosion in MX80 bentonite at 120°C, Materials and Corrosion. 72 (2021) 120–130. https://doi.org/10.1002/maco.202011777.
[27] L. Galai, L. Marchetti, F. Miserque, P. Frugier, N. Godon, E. Brackx, C. Remazeilles, P. Refait, Effect of dissolved Si on the corrosion of iron in deaerated and slightly alkaline solutions (pH ≈ 8.1) at 50 °C, Corrosion Science. 210 (2023) 110790. https://doi.org/10.1016/j.corsci.2022.110790.
[28] J. Owen, F. Ropital, G.R. Joshi, J. Kittel, R. Barker, Galvanic effects induced by siderite and cementite surface layers on carbon steel in aqueous CO2 environments, Corrosion Science. 209 (2022) 110762. https://doi.org/10.1016/j.corsci.2022.110762.
[29] M.L. Schlegel, C. Bataillon, K. Benhamida, C. Blanc, D. Menut, J.-L. Lacour, Metal corrosion and argillite transformation at the water-saturated, high-temperature iron–clay interface: A microscopic-scale study, Applied Geochemistry. 23 (2008) 2619–2633. https://doi.org/10.1016/j.apgeochem.2008.05.019.
[30] C. Rivard, E. Montargès-Pelletier, D. Vantelon, M. Pelletier, C. Karunakaran, L.J. Michot, F. Villieras, N. Michau, Combination of multi-scale and multi-edge X-ray spectroscopy for investigating the products obtained from the interaction between kaolinite and metallic iron in anoxic conditions at 90 °C, Phys Chem Minerals. 40 (2013) 115–132. https://doi.org/10.1007/s00269-012-0552-6.
[31] P. Dillmann, S. Gin, D. Neff, L. Gentaz, D. Rebiscoul, Effect of natural and synthetic iron corrosion products on silicate glass alteration processes, Geochimica et Cosmochimica Acta. 172 (2016) 287–305. https://doi.org/10.1016/j.gca.2015.09.033.
[32] C. Carrière, P. Dillmann, E. Foy, D. Neff, J.J. Dynes, Y. Linard, N. Michau, C. Martin, Use of nanoprobes to identify iron-silicates in a glass/iron/argillite system in deep geological disposal, Corrosion Science. (2019) 108104. https://doi.org/10.1016/j.corsci.2019.108104.
[33] D.R.G. Mitchell, DiffTools: Electron diffraction software tools for DigitalMicrograph™, Microscopy Research and Technique. 71 (2008) 588–593. https://doi.org/10.1002/jemt.20591.
[34] E. Giffaut, M. Grivé, Ph. Blanc, Ph. Vieillard, E. Colàs, H. Gailhanou, S. Gaboreau, N. Marty, B. Madé, L. Duro, Andra thermodynamic database for performance assessment: ThermoChimie, Applied Geochemistry. 49 (2014) 225–236. https://doi.org/10.1016/j.apgeochem.2014.05.007.
[35] P. Blanc, P. Vieillard, H. Gailhanou, S. Gaboreau, N. Marty, F. Claret, B. Madé, E. Giffaut, ThermoChimie database developments in the framework of cement/clay interactions, Applied Geochemistry. 55 (2015) 95–107. https://doi.org/10.1016/j.apgeochem.2014.12.006.
[36] https://www.thermochimie-tdb.com/, (n.d.).
[37] R.J. Lemire, CHEMICAL THERMODYNAMICS OF IRON: PART 2, (c) OECD 2020, n.d.

[38] S. Grousset, M. Bayle, A. Dauzeres, D. Crusset, V. Deydier, Y. Linard, P. Dillmann, F. Mercier-Bion, D. Neff, Study of iron sulphides in long-term iron corrosion processes: Characterisations of archaeological artefacts, Corrosion Science. 112 (2016) 264–275. https://doi.org/10.1016/j.corsci.2016.07.022.
[39] D.L.A. de Faria, S. Venâncio Silva, M.T. de Oliveira, Raman microspectroscopy of some iron oxides and oxyhydroxides, J. Raman Spectrosc. 28 (1997) 873–878.
[40] Z. Bian, S. Kawi, Preparation, characterization and catalytic application of phyllosilicate: A review, Catalysis Today. 339 (2020) 3–23. https://doi.org/10.1016/j.cattod.2018.12.030.
[41] M. Sassi, C.I. Pearce, P.S. Bagus, E. Arenholz, K.M. Rosso, First-Principles Fe L2,3-Edge and O K-Edge XANES and XMCD Spectra for Iron Oxides, Journal of Physical Chemistry A. 121 (2017) 7613–7618. https://doi.org/10.1021/acs.jpca.7b08392.
[42] S. Guilhem, Spectroscopies vibrationnelles: théorie, aspects pratiques et applications, 2020.
[43] S.M. Butorin, Resonant inelastic X-ray scattering as a probe of optical scale excitations in strongly electron-correlated systems: Quasi-localized view, Journal of Electron Spectroscopy and Related Phenomena. 110 (2000) 213–233. https://doi.org/10.1016/S0368-2048(00)00166-3.
[44] S.J. Brotton, R. Shapiro, G. van der Laan, J. Guo, P.A. Glans, J.M. Ajello, Valence state fossils in Proterozoic stromatolites by L-edge X-ray absorption spectroscopy, Journal of Geophysical Research: Biogeosciences. 112 (2007) 1–11. https://doi.org/10.1029/2006JG000185.
[45] M. Gao, X. Pang, K. Gao, The growth mechanism of CO2 corrosion product films, Corrosion Science. 53 (2011) 557–568. https://doi.org/10.1016/j.corsci.2010.09.060.
[46] J. Han, S. Nešić, Y. Yang, B.N. Brown, Spontaneous passivation observations during scale formation on mild steel in CO2 brines, Electrochimica Acta. 56 (2011) 5396–5404. https://doi.org/10.1016/j.electacta.2011.03.053.
[47] H. Lotz, Mécanismes de corrosion du fer en milieu anoxique: caractérisation multi-échelle des propriétés physico-électrochimiques des couches de produits de corrosion., Université Paris-Saclay, 2020.
[48] M.L. Schlegel, S. Necib, S. Daumas, C. Blanc, E. Foy, N. Trcera, A. Romaine, Microstructural characterization of carbon steel corrosion in clay borehole water under anoxic and transient acidic conditions, Corrosion Science. 109 (2016) 126–144. https://doi.org/10.1016/j.corsci.2016.03.022.
[49] D. Burkle, R. De Motte, W. Taleb, A. Kleppe, T. Comyn, S.M. Vargas, A. Neville, R. Barker, In situ SR-XRD study of FeCO3 precipitation kinetics onto carbon steel in CO2-containing environments: The influence of brine pH, Electrochimica Acta. 255 (2017) 127–144. https://doi.org/10.1016/j.electacta.2017.09.138.
[50] M.L. Schlegel, C. Bataillon, C. Blanc, D. Pret, E. Foy, Anodic Activation of Iron Corrosion in Clay Media under WaterSaturated Conditions at 90 °C: Characterization of the Corrosion Interface, Environmental Science & Technology. 44 (2010) 1503–1508. https://doi.org/10.1021/es9021987.
[51] Y. Leon, M. Saheb, E. Drouet, D. Neff, E. Foy, E. Leroy, J.J. Dynes, P. Dillmann, Interfacial layer on archaeological mild steel corroded in carbonated anoxic environments studied with coupled micro and nano probes, Corrosion Science. 88 (2014) 23–35. https://doi.org/10.1016/j.corsci.2014.07.005.
[52] J. Han, D. Young, H. Colijn, A. Tripathi, S. Nešić, Chemistry and Structure of the Passive Film on Mild Steel in CO2 Corrosion Environments, Ind. Eng. Chem. Res. 48 (2009) 6296–6302. https://doi.org/10.1021/ie801819y.
[53] J. Han, B.N. Brown, D. Young, S. Nešić, Mesh-capped probe design for direct pH measurements at an actively corroding metal surface, J Appl Electrochem. 40 (2010) 683–690. https://doi.org/10.1007/s10800-009-0043-8.
[54] A. Michelin, E. Drouet, E. Foy, J.J. Dynes, D. Neff, P. Dillmann, Investigation at the nanometre scale on the corrosion mechanisms of archaeological ferrous artefacts by STXM, J. Anal. At. Spectrom. 28 (2013) 59–66. https://doi.org/10.1039/C2JA30250K.

[55] C. Mansour, G. Berger, M. Fédoroff, G. Lefèvre, A. Pages, E.M. Pavageau, H. Catalette, S. Zanna, Influence of temperature and reducing conditions on the sorption of sulfate on magnetite, Journal of Colloid and Interface Science. 352 (2010) 476–482. https://doi.org/10.1016/j.jcis.2010.08.014.
[56] Y. El Mendili, A. Abdelouas, A. Ait Chaou, J.-F. Bardeau, M.L. Schlegel, Carbon steel corrosion in clay-rich environment, Corrosion Science. 88 (2014) 56–65. https://doi.org/10.1016/j.corsci.2014.07.020.
[57] M.-Y. Lin, Y.-H. Chen, J.-J. Lee, H.-S. Sheu, Reaction pathways of iron-sulfide mineral formation: an in situ X-ray diffraction study, European Journal of Mineralogy. 30 (2018) 77–84. https://doi.org/10.1127/ejm/2017/0029-2681.
[58] J.-A. Bourdoiseau, M. Jeannin, C. Rémazeilles, R. Sabot, P. Refait, The transformation of mackinawite into greigite studied by Raman spectroscopy: Transformation of mackinawite into greigite, J. Raman Spectrosc. 42 (2011) 496–504. https://doi.org/10.1002/jrs.2729.
[59] B.W.A. Sherar, P.G. Keech, D.W. Shoesmith, The effect of sulfide on the aerobic corrosion of carbon steel in near-neutral pH saline solutions, Corrosion Science. 66 (2013) 256–262. https://doi.org/10.1016/j.corsci.2012.09.027.
[60] S. Necib, Y. Linard, D. Crusset, N. Michau, S. Daumas, E. Burger, A. Romaine, M.L. Schlegel, Corrosion at the carbon steel-clay borehole water and gas interfaces at 85 °C under anoxic and transient acidic conditions, Corrosion Science. 111 (2016) 242–258. https://doi.org/10.1016/j.corsci.2016.04.039.
[61] J.L. Crolet, N. Thevenot, S. Nesic, Role of Conductive Corrosion Products in the Protectiveness of Corrosion Layers, CORROSION. 54 (1998) 194–203. https://doi.org/10.5006/1.3284844.
[62] R. De Motte, R. Mingant, J. Kittel, F. Ropital, P. Combrade, S. Necib, V. Deydier, D. Crusset, Near surface pH measurements in aqueous CO2 corrosion, Electrochimica Acta. 290 (2018) 605–615. https://doi.org/10.1016/j.electacta.2018.09.117.
[63] T. Tanupabrungsun, D. Young, B. Brown, S. Nesic, Construction and verification of Pouraix diagrams for CO2 corrosion of mild steel valid up to 250°C, CORROSION. (2012).